

An Asymptotically Exact Reduced PDE Model for the Magnetorotational Instability: Derivation and Numerical Simulations

Ben Jamroz¹, Keith Julien¹ and Edgar Knobloch²

¹ Department of Applied Mathematics, University of Colorado, Boulder, CO 80309, USA

² Department of Physics, University of California, Berkeley, CA 94720, USA

E-mail: keith.julien@colorado.edu

Abstract. Taking advantage of disparate spatio-temporal scales relevant to astrophysics and laboratory experiments, we derive asymptotically exact reduced PDE models for the magnetorotational instability. These models extend recent single-mode formulations leading to saturation in the presence of weak dissipation, and are characterized by a back-reaction on the imposed shear. Numerical simulations performed for a broad class of initial conditions indicate an initial phase of growth dominated by the optimal (fastest growing) magnetorotational instability fingering mode, followed by a vertical coarsening to a box-filling mode.

PACS numbers:

Submitted to: *Physica Scripta*

1. Introduction

Accretion disks occur widely in astrophysics, and are found in binary star systems, protoplanetary systems, as well as near black holes at the center of spiral galaxies. However, accretion can only occur in the presence of an efficient mechanism for angular momentum extraction. Typical (thin) accretion disks are hydrodynamically stable since the specific angular momentum increases outwards. Although turbulence may exist due to finite amplitude perturbations [1, 2, 3, 4, 5], the transfer of angular momentum by the resulting eddy diffusivity appears to be insufficient to support observed accretion rates [6].

The magnetorotational instability (hereafter MRI) present in magnetized accretion disks is a linear axisymmetric instability that grows on the dynamical time scale $\tau_{MRI}^* \sim (\Omega^*)^{-1}$ whenever a poloidal magnetic field is present. Here Ω^* is the characteristic angular velocity of the accreting matter. Although originally discovered by Velikhov [7] and Chandrasekhar [8], it was Balbus & Hawley [9] who first demonstrated that the MRI provides an efficient mechanism for the extraction of angular momentum from ionized accretion disks with angular velocity decreasing outward, $d\Omega^*/dr^* < 0$. When the imposed poloidal magnetic field (with associated Alfvén speed v_A^*) is weak, the instability has small wavelength in the direction parallel to the rotation axis and takes the form of a vertical stack of thin sheets of matter moving alternately radially inwards and outwards [9, 10]. The efficiency of the resulting angular momentum transport depends on the amplitude at which the MRI saturates [11]. Thus the saturation of the MRI is a central question in accretion disk theory.

Since its rediscovery by Balbus and Hawley, the MRI has been the subject of a number of different numerical simulations. Early simulations [9] examined the nonlinear evolution of the axisymmetric instability within a local formulation, focusing on compressible disks but ignoring their vertical structure and explicit dissipation. In these simulations the background flow is reduced to a Couette flow, and Cartesian coordinates are used with periodic boundary conditions in the vertical direction. Subsequent simulations with explicit resistivity (but no explicit viscosity) within the shearing sheet formulation [12] revealed that the MRI saturates via ohmic diffusivity η^* when the Elsasser number $\Lambda \equiv v_A^{*2}/\eta^*\Omega^*$ is of order one or less, but found that for larger Λ the instability continues to grow, apparently without saturation. Fleming *et al* [13] subsequently showed, following the suggestion that secondary (‘parasitic’) shear instabilities of the moving sheets could lead to saturation [14], that the MRI does apparently saturate if nonaxisymmetric instabilities are included, with the magnetic energy in the final state somewhat smaller than the initial thermal energy in the disk. Thus in all cases the computations indicate that the disk remains supported in the radial direction by thermal pressure. Recent simulations have endeavored to make the models more realistic by including the vertical structure of the disk as well as other effects, but the saturation mechanism for the axisymmetric MRI remains unresolved.

The problem is characterized by three distinct time scales: the fast rotational time

scale, a moderate Alfvén time scale and a slow dissipative time scale. This large range of scales makes the problem difficult to simulate in a direct numerical simulation, since one must integrate over at least one dissipative time scale to reach saturation. On the other hand this disparity in time scales can be used to construct a self-consistent asymptotic description [11] that allows us to explore the saturation of the instability.

In order to extract the essence of the problem we adopt the model considered originally by Balbus and Hawley [9], i.e., we take a local model of a disk with homogeneous structure in both the radial and axial directions, and constant imposed toroidal and poloidal magnetic fields. We assume for simplicity that the flow is incompressible, but include explicitly both ohmic and viscous dissipation.

2. Problem Formulation

To describe the local dynamics of the MRI occurring within a cylindrical geometry we select a reference frame a distance r^* from the central axis and suppose that this frame rotates with the local angular velocity $\boldsymbol{\Omega}^* = \Omega^*(r^*)\hat{\mathbf{z}}$. The equations of motion for a rotating electrically conducting viscous incompressible fluid are

$$\begin{aligned} \mathbf{u}_{t^*}^* + \mathbf{u}^* \cdot \nabla^* \mathbf{u} + 2\boldsymbol{\Omega}^* \times \mathbf{u}^* &= -\frac{1}{\rho^*} \nabla^* p^* - \frac{1}{2\mu_0 \rho^*} \nabla^* |\mathbf{B}^*|^2 + \frac{1}{\mu_0 \rho^*} \mathbf{B}^* \cdot \nabla^* \mathbf{B}^* \\ &\quad + \nu^* \nabla^{*2} \mathbf{u}^*, \\ \mathbf{B}_{t^*}^* + \mathbf{u}^* \cdot \nabla^* \mathbf{B}^* &= \mathbf{B}^* \cdot \nabla^* \mathbf{u}^* + \eta^* \nabla^{*2} \mathbf{B}^*, \\ \nabla^* \cdot \mathbf{u}^* &= \nabla^* \cdot \mathbf{B}^* = 0. \end{aligned}$$

Here ρ^* is the density, and ν^* and η^* are, respectively, the kinematic viscosity and ohmic diffusivity, all assumed constant. We choose (x^*, y^*, z^*) as local Cartesian coordinates with x^* pointing in the radial direction, y^* in the azimuthal direction and z^* parallel to the rotation axis. In this local approximation we may assume a straight channel geometry $-L^*/2 \leq x^* \leq L^*/2$, $-\infty \leq y^* \leq \infty$, $-\infty \leq z^* \leq \infty$, and suppose that the azimuthal shear is locally linear, $\mathbf{U}_0 = (0, \sigma^* x, 0)$, $\sigma^* < 0$, and that a constant magnetic field $\mathbf{B}_0 = (0, B_{tor}^*, B_{pol}^*)$ is present. In thin accretion disks the rotation rate $\Omega^*(r^*)$ is determined by the primary Kepler balance $r^* \Omega^{*2} = GM^*/r^{*2}$. However, in a laboratory setting $\Omega^*(r^*)$ is set by external boundary conditions, i.e., differentially rotating outer and inner cylinders.

In the following we non-dimensionalize these equations using a velocity scale U^* , a length scale L^* , and B_{pol}^* as the magnetic field scale; the corresponding dimensionless quantities are indicated by the absence of the superscript $*$. Thus $\mathbf{u}^* = (u^*, v^*, w^*) = U^*(u, v, w)$, $\mathbf{b}^* = (a^*, b^*, c^*) = B_{pol}^*(a, b, c)$. In addition it is convenient to introduce the meridional stream function ψ and the meridional flux function ϕ such that $(u, v, w) = (-\psi_z, v, \psi_x)$, $(a, b, c) = (-\phi_z, b, \phi_x)$. The axisymmetric equations then take the dimensionless form

$$\nabla^2 \psi_t + 2\Omega v_z + J(\psi, \nabla^2 \psi) = v_A^2 \nabla^2 \phi_z + v_A^2 J(\phi, \nabla^2 \phi) + \nu \nabla^4 \psi, \quad (1)$$

$$v_t - (2\Omega + \sigma)\psi_z + J(\psi, v) = v_A^2 b_z + v_A^2 J[\phi, b] + \nu \nabla^2 v, \quad (2)$$

$$\phi_t + J(\psi, \phi) = \psi_z + \eta \nabla^2 \phi, \quad (3)$$

$$b_t + J(\psi, b) = v_z - \sigma \phi_z + J(\phi, v) + \eta \nabla^2 b, \quad (4)$$

where $v_A^2 \equiv B_{pol}^*/\mu_0\rho^*U^{*2}$ is the square of the dimensionless Alfvén speed associated with the vertical (poloidal) magnetic field, $J(f, g) \equiv f_x g_z - f_z g_x$, and $\Omega \equiv \Omega^* L^*/U^*$, $\sigma \equiv \sigma^* L^*/U^*$, $\nu \equiv \nu^*/U^* L^*$, and $\eta \equiv \eta^*/U^* L^*$ are the dimensionless rotation rate, shear rate, kinematic viscosity, and ohmic diffusivity. Note that B_{tor} drops out of these equations. This is not so in an annulus, where hoop stresses are present, and the MRI becomes oscillatory [15, 16]. Furthermore, invariance under reflection $x \rightarrow -x$, $(\psi, v, \phi, b) \rightarrow -(\psi, v, \phi, b)$ implies no distinction between inward and outward directions. Consequently, in this local model the direction of accretion and of (angular) momentum flux must be imposed externally.

2.1. Linear Theory

Equations (1)-(4), linearized about the trivial state $\psi = v = \phi = b = 0$, yield the dispersion relation

$$p[(\lambda + \nu p)(\lambda + \eta p) + v_A^2 n^2]^2 + 2\Omega n^2[(\lambda + \eta p)^2(2\Omega + \sigma) + \sigma v_A^2 n^2] = 0, \quad (5)$$

where $p \equiv k^2 + n^2$ and λ is the growth rate of perturbations of the form $\exp(ikx + inz)$. This equation yields positive growth rates for a finite interval of vertical wavenumbers n whenever $\sigma < 0$, $v_A \neq 0$, provided only that ν and η are sufficiently small [9]. Equation (5) also yields an expression for the threshold for the instability, i.e., $\lambda = 0$, which may be interpreted as defining a critical Elsasser number $\Lambda \equiv v_A^2/\Omega\eta$, namely,

$$\Lambda_c = - \left[\nu\eta p^3 + \Omega\sigma n^2 + \sqrt{\Omega^2\sigma^2 n^4 + 2\Omega n^2 p^3 \eta(\sigma\nu - (2\Omega + \sigma)\eta)} \right] / p\Omega\eta. \quad (6)$$

3. Derivation of the Reduced Equations

In this section we extend the asymptotic analysis of Eqs. (1)-(4) by Julien & Knobloch [17, 11, 18] in two ways: we allow for independent scaling of the dissipative processes and the driving rotation and shear,

$$(\nu, \eta) = \epsilon(\hat{\nu}, \hat{\eta}), \quad (\Omega, \sigma) = \delta^{-1}(\hat{\Omega}, \hat{\sigma}), \quad (n, \lambda) = \delta^{-1}(\hat{n}, \hat{\lambda}), \quad (7)$$

where $\epsilon \ll 1$, $\delta \ll 1$, and for multiple scales in the x direction required to accommodate lateral boundary conditions. Specifically, we propose a multiple scales expansion in x with ∂_x replaced by $\delta^{-1}\partial_x + \partial_X$, where $X = \delta x$. In addition vertical derivatives are large, $\partial_z \rightarrow \delta^{-1}\partial_z$, as are time derivatives $\partial_t \rightarrow \delta^{-1}\partial_t$. In all cases we choose the characteristic scales by taking $v_A^2 \equiv 1$.

In parallel with the above assumptions, we need to make further assumptions about the relative magnitude of the various fields. The rapid shearing by the azimuthal flow suggests that we take $(\psi, \phi) \rightarrow \delta^{1/2}\epsilon^{1/2}(\psi, \phi)$ and $(v, b) \rightarrow \delta^{-1}(v, b)$. Existing results for strongly nonlinear solutions [17, 11, 18] are recovered on letting $\delta \rightarrow \epsilon$.

We find it convenient to separate the fields into mean and fluctuating components,

$$f(x, X, z, t) = \overline{f}(X) + f'(x, X, z, t), \quad \overline{f'} = 0,$$

where the overbar denotes the average in both space and time,

$$\overline{f}(X) := \lim_{\tau, V \rightarrow \infty} \frac{1}{\tau V} \int_{\tau, V} f(x, z, X, t) dx dz dt.$$

Averaging Eqs. (2) and (4) yields the mean azimuthal equations

$$\epsilon^{\frac{1}{2}} \delta^{\frac{1}{2}} \overline{J_X(\psi, v)} = \epsilon^{\frac{1}{2}} \delta^{\frac{1}{2}} v_A^2 \overline{J_X(\phi, b)} + \epsilon \delta \widehat{\nu} \partial_X^2 \overline{v}, \quad (8)$$

$$\epsilon^{\frac{1}{2}} \delta^{\frac{1}{2}} \overline{J_X(\psi, b)} = \epsilon^{\frac{1}{2}} \delta^{\frac{1}{2}} \overline{J_X(\phi, v)} + \epsilon \delta \widehat{\eta} \partial_X^2 \overline{b}, \quad (9)$$

where $J_X(f, g) \equiv \partial_X f \partial_z g - \partial_z f \partial_X g$. The fluctuating equations are

$$\widetilde{\nabla}^2 \psi'_t + (\epsilon \delta)^{-\frac{1}{2}} 2\widehat{\Omega} v'_z + \left(\frac{\epsilon}{\delta}\right)^{\frac{1}{2}} J_x(\psi', \widetilde{\nabla}^2 \psi') = v_A^2 \widetilde{\nabla}^2 \phi'_z + \quad (10)$$

$$\left(\frac{\epsilon}{\delta}\right)^{\frac{1}{2}} v_A^2 J_x(\phi', \widetilde{\nabla}^2 \phi') + \left(\frac{\epsilon}{\delta}\right) \widehat{\nu} \widetilde{\nabla}^4 \psi' + \mathcal{O}((\epsilon \delta)^{\frac{1}{2}}, \delta),$$

$$v'_t - (\epsilon \delta)^{\frac{1}{2}} (2\widehat{\Omega} + \widehat{\sigma}) \psi'_z + \left(\frac{\epsilon}{\delta}\right)^{\frac{1}{2}} (J_x(\psi', v') + \delta (J_X(\psi, v) - \overline{J_X(\psi, v)})) \quad (11)$$

$$v_A^2 b'_z + \left(\frac{\epsilon}{\delta}\right)^{\frac{1}{2}} v_A^2 (J_x(\phi', b') + \delta (J_X(\phi, b) - \overline{J_X(\phi, b)})) + \left(\frac{\epsilon}{\delta}\right) \widehat{\nu} \widetilde{\nabla}^2 v',$$

$$\phi'_t + \left(\frac{\epsilon}{\delta}\right)^{\frac{1}{2}} J_x(\psi', \phi') = \psi'_z + \left(\frac{\epsilon}{\delta}\right) \widehat{\eta} \widetilde{\nabla}^2 \phi' + \mathcal{O}((\epsilon \delta)^{\frac{1}{2}}, \delta), \quad (12)$$

$$b'_t + \left(\frac{\epsilon}{\delta}\right)^{\frac{1}{2}} (J_x(\psi', b') + \delta (J_X(\psi, b) - \overline{J_X(\psi, b)})) = v'_z - (\epsilon \delta)^{\frac{1}{2}} \widehat{\sigma} \phi'_z + \quad (13)$$

$$\left(\frac{\epsilon}{\delta}\right)^{\frac{1}{2}} (J_x(\phi', v') + \delta (J_X(\phi, v) - \overline{J_X(\phi, v)})) + \left(\frac{\epsilon}{\delta}\right) \widehat{\eta} \widetilde{\nabla}^2 b',$$

where $J_x(f, g) \equiv \partial_x f \partial_z g - \partial_z f \partial_x g$, $\nabla \equiv \widetilde{\nabla} + \delta \widehat{x} \partial_X$ and $\widetilde{\nabla} \equiv (\partial_x, 0, \partial_z)$.

We now expand the variables ψ, v, ϕ, b in terms of the small parameters ϵ, δ in the form $\psi = \sum_{i,j} \epsilon^{i/2} \delta^{j/2} \psi_{ij}$ with similar expressions for the other three fields. From Eqs. (10-13) we obtain $v'_{0j} = b'_{0j} \equiv 0$ to all orders. Given this fact and that $v'_{10} = 0$ from $\mathcal{O}(\epsilon^{-1/2} \delta^{-1/2})$ in (10) and $b_{10} = 0$ in (11) and (13) at $\mathcal{O}(\epsilon^{1/2})$, we find that the first nontrivial balances occur at $\mathcal{O}(1)$ in (10) and (12) and $\mathcal{O}(\epsilon^{1/2} \delta^{1/2})$ in (11) and (13). The reduced fluctuating equations are

$$\widetilde{\nabla}^2 \psi'_{00t} + 2\widehat{\Omega} v'_{11z} + \left(\frac{\epsilon}{\delta}\right)^{\frac{1}{2}} J_x(\psi'_{00}, \widetilde{\nabla}^2 \psi'_{00}) = v_A^2 \widetilde{\nabla}^2 \phi'_{00z} + \quad (14)$$

$$v_A^2 \left(\frac{\epsilon}{\delta}\right)^{\frac{1}{2}} J_x(\phi'_{00}, \widetilde{\nabla}^2 \phi'_{00}) + \left(\frac{\epsilon}{\delta}\right) \widehat{\nu} \widetilde{\nabla}^4 \psi'_{00},$$

$$v'_{11t} - (2\widehat{\Omega} + \widehat{\sigma} + \partial_X \overline{v}_{00}) \partial_z \psi'_{00} + \left(\frac{\epsilon}{\delta}\right)^{\frac{1}{2}} J_x(\psi'_{00}, v'_{00}) = \quad (15)$$

$$v_A^2 \left(b'_{11z} - \partial_X \overline{b}_{00} \phi'_{00z} + \left(\frac{\epsilon}{\delta}\right)^{\frac{1}{2}} J_x(\phi'_{00}, b'_{00}) \right) + \left(\frac{\epsilon}{\delta}\right) \widehat{\nu} \widetilde{\nabla}^2 v'_{11},$$

$$\phi'_{00t} + \left(\frac{\epsilon}{\delta}\right)^{\frac{1}{2}} J_x(\psi'_{00}, \phi'_{00}) = \psi'_{00z} + \left(\frac{\epsilon}{\delta}\right) \hat{\eta} \widetilde{\nabla}^2 \phi'_{00}, \quad (16)$$

$$b'_{11t} - \partial_X \bar{b}_{00} \psi'_{00z} + \left(\frac{\epsilon}{\delta}\right)^{\frac{1}{2}} J_x(\psi'_{00}, b'_{11}) = v'_{11z} - (\hat{\sigma} + \partial_X \bar{v}_{00}) \phi'_{00z} + \left(\frac{\epsilon}{\delta}\right)^{\frac{1}{2}} J_x(\phi'_{00}, v'_{11}), + \left(\frac{\epsilon}{\delta}\right) \hat{\eta} \widetilde{\nabla}^2 b'_{11}. \quad (17)$$

Thus nonlinear and dissipative terms are retained at leading order when $\delta = \epsilon$ (Case A) but become subdominant when $\epsilon \ll \delta \ll 1$ (Case B). Closure of the reduced fluctuating equations (14)-(17) requires the determination of $\partial_X \bar{v}_{00}$ and $\partial_X \bar{b}_{00}$. Nontrivial balances in the mean equations (8) and (9) first arise at $\mathcal{O}(\epsilon\delta)$ giving

$$\hat{\nu} \partial_{XX} \bar{v}_{00} = -\partial_X \left(\overline{\psi'_{00z} v'_{11}} - v_A^2 \overline{\phi'_{00z} b'_{11}} \right), \quad (18)$$

$$\hat{\eta} \partial_{XX} \bar{b}_{00} = -\partial_X \left(\overline{\psi'_{00z} b'_{11}} - \overline{\phi'_{00z} v'_{11}} \right). \quad (19)$$

We are permitted to integrate once to obtain explicitly the quantities needed to close the system,

$$\hat{\nu} \partial_X \bar{v}_{00} = -\overline{\psi'_{00z} v'_{11}} + v_A^2 \overline{\phi'_{00z} b'_{11}} \equiv \overline{u'_{00} v'_{11}} - v_A^2 \overline{a'_{00} b'_{11}}, \quad (20)$$

$$\hat{\eta} \partial_X \bar{b}_{00} = -\overline{\psi'_{00z} b'_{11}} + \overline{\phi'_{00z} v'_{11}} + C \equiv \overline{u'_{00} b'_{11}} - \overline{a'_{00} v'_{11}} + C, \quad (21)$$

where the constant C is determined by radial force balance across the channel in the saturated state. Note that with this closure for $\partial_X \bar{v}_{00}$ and $\partial_X \bar{b}_{00}$, there is no coupling via a large scale derivative in X , thus \bar{v}_{00} and \bar{b}_{00} are linear functions in X . Furthermore, note that \bar{v}_{00} is directly related to the angular momentum transfer of the system, through the xy component of the stress tensor,

$$T_{xy} \equiv u'_{00} v_{11} - a'_{00} b_{11} = -\psi'_{00z} v_{11} + \phi'_{00z} b_{11}.$$

We can therefore evaluate the efficiency of angular momentum transport by examining the quantity $\overline{T}_{xy} = \hat{\nu} \partial_X \bar{v}_{00}$ [19]. Similarly for the mixed stress terms we define

$$M_{xy} \equiv u'_{00} b_{11} - a'_{00} v_{11} = -\psi'_{00z} b_{11} + \phi'_{00z} v_{11},$$

with

$$\overline{M}_{xy} = \hat{\eta} \partial_X \bar{b}_{00} - C.$$

The total volume-averaged energy of the MRI is given by $E(t) \equiv \int (|\widetilde{\nabla} \psi'_{00}|^2 + v_{11}^2) + v_A^2 (|\widetilde{\nabla} \phi'_{00}|^2 + b_{11}^2) dx dz$. If saturation occurs in the reduced model, total energy $|E(t)|$ is bounded and $\overline{\partial_t E(t)} \rightarrow 0$. The energy balance for the reduced system then enforces the global constraint at saturation

$$- (\hat{\sigma} + \partial_X \bar{v}_{00}) \hat{\nu} \partial_X \bar{v}_{00} - v_A^2 \partial_X \bar{b}_{00} (\hat{\eta} \partial_X \bar{b}_{00} - C) - \left(\frac{\epsilon}{\delta}\right) \left[\hat{\nu} \left(\overline{(\widetilde{\nabla}^2 \psi'_{00})^2 + |\widetilde{\nabla} v'_{11}|^2} \right) + \hat{\eta} \left(\overline{(\widetilde{\nabla}^2 \phi'_{00})^2 + |\widetilde{\nabla} b'_{11}|^2} \right) \right] = 0. \quad (22)$$

The mean azimuthal flow shear generated by the MRI serves to counteract the ambient shear, i.e., $\partial_X \bar{v}_{00} > 0$. The first term is thus positive definite and so is balanced by the remaining three terms. Of these the third and fourth terms are negative definite,

while the second term is only negative definite if $\partial_X \bar{b}_{00}$ and \bar{M}_{xy} are of the same sign. Moreover, since $\bar{M}_{xy} = 0$ for both single mode solutions of (14)-(17) [17, 11, 18] and in the numerical solutions (see below), saturation of the MRI in the energy norm requires the presence of viscous and/or ohmic dissipation.

In the remainder of the paper we consider only Case A, with $\delta = \epsilon$ and $\Lambda \sim \mathcal{O}(1)$.

4. Numerical method for simulation of the reduced equations

The reduced system derived in §3 is solved in a box of size $L_X \times N_z L$, where N_z is the number of vertical wavelengths, L , of the fastest growing linear mode (determined from the scaled linear dispersion relation) and $L_X \sim \epsilon^{-1}$ is now the large scale transverse dimension. We choose periodic boundary conditions in the z direction to simulate a vertically infinite domain. In the x direction, we impose either periodic or stress-free conditions. Periodic boundary conditions in the horizontal are relevant to astrophysical shearing box models, while impenetrable stress-free conditions relate to laboratory experiments [20, 21, 22].

Time integration is performed using the semi-implicit Runge-Kutta method developed by Spalart *et al* [23]. This method is second-order accurate for terms that are treated implicitly (diffusive terms, $\tilde{\nu} \tilde{\nabla}^4 \psi'_{00}$, $\tilde{\nu} \tilde{\nabla}^2 v'_{11}$, $\tilde{\eta} \tilde{\nabla}^2 \phi'_{00}$, and $\tilde{\eta} \tilde{\nabla}^2 b'_{11}$ in our model) and achieves third order accuracy for terms treated explicitly (nonlinear and cross terms). We use a Fourier/trigonometric spatial discretization with the standard 2/3 de-aliasing rule required because of the quadratic nonlinearities in the problem. Closure is obtained by spatially averaging over the small-scales as described in Eqs. (20)-(21). The parameter ϵ relating the large scale X with the small scales (x, z) enters our model implicitly through the size of our computational domain, $L_X = \epsilon^{-1} L$.

5. Results

5.1. Single Mode Theory

Julien & Knobloch [17, 11, 18] established the existence of exact, saturated, single-mode solutions to the reduced equations (14)-(21) for Case A with $\delta = \epsilon$, $\Lambda = \mathcal{O}(1)$. This is in contrast to the requirement $\Lambda \leq 1$ identified by Sano *et. al.* [12] in the absence of viscosity. These single-mode solutions take the x -invariant form

$$\psi'_{00} \equiv \cos(nz)\psi'_0(t), \quad v'_{11} \equiv \sin(nz)v'_1(t), \quad \phi'_{00} \equiv \sin(nz)\phi'_0(t), \quad b'_{11} \equiv \cos(nz)b'_1(t)$$

together with mean field shear profiles

$$\partial_X \bar{v}_{00} \equiv V'(X), \quad \partial_X \bar{b}_{00} \equiv B'(X).$$

Thus all Jacobian nonlinear terms in (14)-(17) are identically zero and the only surviving nonlinearities arise solely through interactions between fluctuating and mean quantities. Using the resulting nonlinear dispersion relation, as defined in [11], one is able to obtain explicit formulae for the steady-state saturated values of amplitudes $\psi'_0, v'_0, \phi'_0, b'_0$ and

the associated mean field responses $V'(X)$, $B'(X)$. For these solutions $\overline{M}_{xy} \equiv 0$ owing to their parity in the z direction. Specifically, if $C = 0$ it follows that $B'(X) \equiv 0$. We have used these exact results to test the code.

Each simulation is started with the above initial conditions, with the vertical wavenumber n chosen to maximize the linear theory growth rate. Periodic boundary conditions are imposed in the radial direction. With no mechanism to modify the initial wavenumber, only this wavenumber is present for the length of the computation. Therefore, the fields ψ'_{00} , b'_{11} remain 90° out of phase with v'_{11} , ϕ'_{00} throughout the approach to saturation. The growth rate λ is calculated by fitting the growth of the global quantity $V'(X)$ while the instability is still in the kinematic phase (figure 1). Sample results for various parameter values versus the single mode theory are shown in figure 2.

5.2. Stress-free Boundary Conditions

With periodic boundary conditions and a monochromatic vertical mode given by the linear dispersion relation the MRI instability evolves as a single-mode solution as described in [17, 11]. However, recent laboratory experiments require the inclusion of impenetrable boundary conditions in the radial direction. For simplicity and efficiency in our numerical approach we use stress-free boundary conditions in the x direction for which a complete Fourier pseudospectral algorithm is possible. The boundary conditions are responsible for the presence of boundary layers which match with the solution in the interior of the domain.

In the following simulations we use a spatially modulated monochromatic mode as initial condition, viz.,

$$\begin{aligned}\psi'_{00} &\equiv \cos(nz) \sin(\pi x/L_x) \psi_0, & v'_{11} &\equiv \sin(nz) \sin(\pi x/L_x) v_1, \\ \phi'_{00} &\equiv \sin(nz) \sin(\pi x/L_x) \phi_0, & b'_{11} &\equiv \cos(nz) \sin(\pi x/L_x) b_1,\end{aligned}$$

where L_X is the length of the computational domain in the x direction. The evolution of $V'(X)$ to the saturated state for Keplerian flow, $\widehat{\Omega} = -2/3\widehat{\sigma}$, together with $\widehat{\sigma} = -1$, $\widehat{\eta} = 1$, $\widehat{\nu} = 1$, $v_A = 1$, and $\delta = \epsilon = 0.1$ is shown in figure 3. The saturated state resulting from this initial condition is shown in figure 4. In the interior of the domain, the fields ψ'_{00} , b'_{11} approach a constant value in x and have zero mean in the z direction. The profiles of the z -average of the fields v'_{11} and ϕ'_{00} are shown in figure 5. Modulo their mean, these fields resemble those obtained with periodic boundary conditions, and remain out of phase with ψ'_{00} , b'_{11} .

Since we are now allowing for boundary effects, the nonlinear dispersion relation used to calculate $V'(X)$ and $\|\psi'_{00}\|_{L^\infty}$ cannot predict the correct saturated values of these quantities. Figure 6 compares the numerically obtained values against the asymptotic results when $\epsilon = 0.1$. We see that the numerically calculated $V'(X)$, which is of primary interest, is still well predicted by the asymptotic single mode theory. The growth rates differ, however, since the growth of modes with horizontal structure is no

longer predicted by the single mode asymptotics. In addition, the values for ψ'_{00} are now dominated by boundary effects. The rms in z of ψ'_{00} for $\hat{\sigma} = -1$ and a range of values of $\hat{\eta}$ is shown in figure 7, where the penetration of boundary effects can be seen.

5.3. Other Initial Conditions

For more robust exploration of the saturation process, we now look at a sample of different initial conditions. We do not begin the simulations with the fastest growing eigenfunction, but pick initial conditions with no bias for this (or any other) mode, and allow it to grow naturally.

We first look at an initial ϕ'_{00} in the form of a Gaussian in the center (in x) of the domain corresponding to a spatially localized vertical magnetic field. The other variables are initialized with $v'_{11} = b'_{11} = 0$ with ψ'_{00} as a small pseudorandom perturbation. The computational domain is set up to allow 16 of the fastest growing linear wavelengths in the z direction and 10 times this wavelength in the x direction. The evolution of ϕ'_{00} is shown in figure 8. At the beginning of the simulation the instability is in its kinematic stage, and the dominant structure is indeed the fastest growing linear mode (figure 8b). As the solution evolves and the flow saturates, nonlinear interactions send energy to smaller wavenumbers and the flow coarsens to the largest wavelength supported by the domain.

For comparison, figure 9 shows the evolution of ϕ'_{00} starting from a small perturbation ψ'_{00} and $\phi'_{00} = v'_{11} = b'_{11} = 0$. As before, the fastest growing linear wavenumber dominates the flow in the kinematic stage. As saturation is approached, the flow coarsens to larger and larger wavelengths in the vertical direction until the flow is dominated by the lowest vertical wavenumber supported on the computational domain.

The single mode theory as presented by Julien & Knobloch in [11] predicts this coarsening of the flow to the lowest wavenumber supported by the computational domain. Although an initially random field has no bias towards the single mode theory and includes a mixture of many modes, the value of $V'(X)$ for the coarsened, saturated flow matches the single mode theory for a mode with the largest wavelength supported by the computational domain. The saturated values of $V'(X)$ with random initial conditions with varying vertical box lengths are shown in figure 10 and follow the single mode theory.

5.4. Statistics

The transport of angular momentum is the primary reason for studying the saturation of the MRI instability. Sano *et al* [12] found that magnetic Reynolds stresses dominate Reynolds stresses in the transport of angular momentum, a conclusion confirmed in figure 11 for various values of $\hat{\eta}$ when $\hat{\sigma} = -1$, $\hat{\Omega} = -2/3\hat{\sigma}$, $\hat{\nu} = 1$, $v_A = 1$ and $\epsilon = 0.1$. We also find, consistent with the single-mode investigations of [11], that while

the values of the fluctuating quantities increase with $\hat{\eta}$ the back-reaction $V'(X)$ saturates (figure 11).

Finally, we may associate a turbulent viscosity with the fully developed MRI using the estimate $\nu_t \sim uL_z$, $L_z \sim 2\pi\epsilon/n$. Thus $\nu_t \sim 2\pi\epsilon\|\psi'_{00}\|_{L^\infty}$ and the turbulent viscosity is of order ϵ .

6. Conclusion

In this work we derived and simulated a new class of asymptotic partial differential equations describing the evolution of the MRI. These reduced equations take advantage of disparate spatio-temporal scales relevant to astrophysical disks and laboratory experiments namely: $t_\Omega \sim \Omega^{-1} \ll 1$, $t_{v_A} \sim \mathcal{O}(1)$, $t_{diss} \gg 1$ and describe the evolution of $\mathcal{O}(\delta)$ wavelength perturbations in z over $\mathcal{O}(\delta^{-1})$ rotation periods. Two classes of reduced equations were identified.

In Case A, where $\epsilon = \delta \ll 1$ and $\Lambda = \mathcal{O}(1)$, dissipative effects lead to saturation of the amplitude of the fingering modes. Numerical simulations show that the single mode theory of Knobloch & Julien [17] captures the essence of the saturation process. In particular the saturated back-reaction on the imposed shear (see figure 10) provides a measure of turbulent angular momentum transport.

In Case B, where $\epsilon \ll \delta \ll 1$ and $\Lambda \gg \mathcal{O}(1)$, dissipative effects are subdominant. Preliminary investigation of the single mode solutions to the reduced pdes (not presented here) shows that $V'(X)$, and thus angular momentum transport, continues to saturate, while the amplitudes of the fluctuating modes grow algebraically in time. In contrast, the amplitude of the inviscid single mode solution of Goodman and Xu [14] grows exponentially. The predictions of this model will be described elsewhere.

References

- [1] F. Wendt. Turbulents Strömungen zwischen zwei rotierenden conaxialen Zylindern. *Ingen. Arch*, 4:577–595, 1933.
- [2] G. I. Taylor. Fluid friction between rotating cylinders. Part I. Torque measurements. *Proc. R. Soc. London A*, 157:546–578, 1936.
- [3] J. Lerner and E. Knobloch. The long-wave instability of a defect in a uniform parallel shear. *J. Fluid Mech.*, 189:117–134, 1988.
- [4] B. Dubrulle, O. Dauchot, F. Daviaud, P.-Y. Longaretti, D. Richard, and J.-P. Zahn. Stability and turbulent transport in Taylor-Couette flow from analysis of experimental data. *Phys. Fluids*, 17:095103/1–19, 2005.
- [5] B. Dubrulle, L. Marié, Ch. Normand, D. Richard, F. Hersant, and J.-P. Zahn. A hydrodynamic shear instability in stratified disks. *Astr. Astrophys.*, 429:1–13, 2005.
- [6] H. Ji, M. Burin, E. Schartman, and J. Goodman. Hydrodynamic turbulence cannot transport angular momentum effectively in astrophysical disks. *Nature*, 444:343–346, 2006.
- [7] E. P. Velikhov. Stability of an ideally conducting liquid flowing between cylinders rotating in a magnetic field. *Sov. Phys. JETP*, 36:1398–1404, 1959.
- [8] S. Chandrasekhar. The hydrodynamic stability of inviscid flow between coaxial cylinders. *PNAS*, 46:253–257, 1960.

- [9] S. A. Balbus and J. F. Hawley. A powerful local shear instability in weakly magnetized disks. I. Linear analysis. *Ap. J.*, 376:214–222, 1991.
- [10] S. A. Balbus and J. F. Hawley. Instability, turbulence, and enhanced transport in accretion disks. *Rev. Mod. Phys.*, 70:1–53, 1998.
- [11] K. Julien and E. Knobloch. Saturation of the magnetorotational instability: Asymptotically exact theory. *EAS Publications Series*, 21:81–104, 2006.
- [12] T. Sano, S. Inutsuka, and S. M. Miyama. A saturation mechanism of magnetorotational instability due to ohmic dissipation. *Ap. J.*, 506:L57–60, 1998.
- [13] T. P. Fleming, J. M. Stone, and J. F. Hawley. The effect of resistivity on the nonlinear stage of the magnetorotational instability in accretion disks. *Ap. J.*, 530:464–477, 2000.
- [14] J. Goodman and G. Xu. Parasitic instabilities in magnetized, differentially rotating disks. *Ap. J.*, 432:213–223, 1994.
- [15] E. Knobloch. On the stability of magnetized accretion discs. *MNRAS*, 255:25–28, 1992.
- [16] E. Knobloch. Symmetry and instability in rotating hydrodynamic and magnetohydrodynamic flows. *Phys. Fluids*, 8:1446–1454, 1996.
- [17] E. Knobloch and K. Julien. Saturation of the magnetorotational instability. *Phys. Fluids*, 17:094106/1–6, 2005.
- [18] K. Julien and E. Knobloch. Reduced models for fluid flows with strong constraints. *J. Math. Phys.*, 48:65405/1–34, 2007.
- [19] A. Mignone, G. Bodo, F. Cattaneo, P. Rossi, and A. Ferrari. Multiple states in magneto-rotational dynamics. *Draft*.
- [20] D. R. Sisan, N. Mujica, W. A. Tillotson, Y.-M. Huang, W. Dorland, A. B. Hassam, T. M. Antonsen, and D. P. Lathrop. Experimental observation and characterization of the magnetorotational instability. *Phys. Rev. Lett.*, 93:114502/1–4, 2004.
- [21] F. Stefani, T. Gundrum, G. Gerbeth, G. Rudiger, M. Schultz, J. Szklarski, and R. Hollerbach. Experimental evidence for magnetorotational instability in a Taylor-Couette flow under the influence of a helical magnetic field. *Phys. Rev. Lett.*, 97(18):184502/1–4, 2006.
- [22] F. Stefani, T. Gundrum, G. Gerbeth, G. Rudiger, J. Szklarski, and R. Hollerbach. Experiments on the magnetorotational instability in helical magnetic fields. *New J. Phys.*, 9(8):295, 2007.
- [23] P. R. Spalart, R. D. Moser, and M. M. Rogers. Spectral methods for the Navier-Stokes equations with one infinite and two periodic directions. *J. Comp. Phys.*, 96:297–324, 1991.

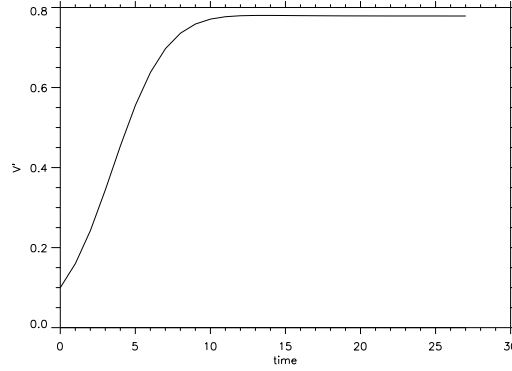


Figure 1. The evolution of $V'(X)$ for $\hat{\sigma} = -1$, $\hat{\Omega} = -2/3\hat{\sigma}$, $\hat{\eta} = 1$, $\hat{\nu} = 1$, $v_A = 1$, and $\delta = \epsilon = 0.1$. Kinematic growth in the early phase is followed by saturation.

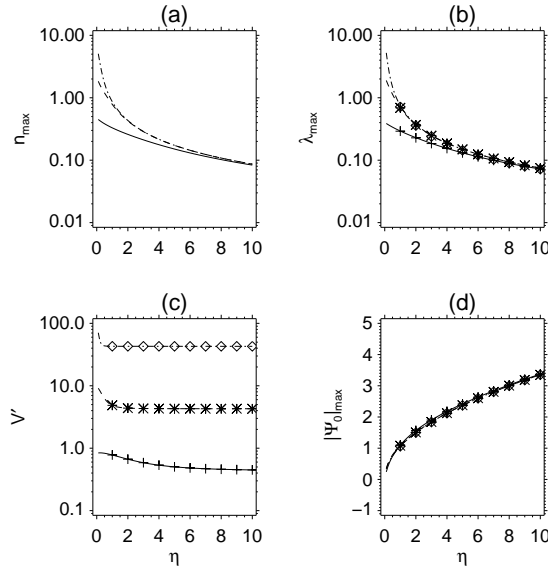


Figure 2. Comparison with single-mode theory. (a) The wavenumber n_{max} of the fastest growing mode, (b) its growth rate λ_{max} , (c) the resulting shear rate $V'(X)$ and (d) the maximum stream function amplitude predicted by the nonlinear dispersion relation with the computed value at the midpoint $|\Psi_0|_{max} \equiv \max_{0 \leq z \leq N_z L} |\psi'_{00}(LX/2, z, t_\infty)|$, as functions of $\hat{\eta}$ for $\hat{\Omega} = -2/3\hat{\sigma}$, $\hat{\nu} = 1$, $v_A = 1$ and $\hat{\sigma} = -100, -10, -1$ (dashed-dot, dashed, solid). The numerical results with diamonds, asterisks and crosses representing $\hat{\sigma} = -100, -10, -1$, respectively, are superposed on the analytical predictions of Knobloch & Julien [17]. The choice of the computational domain to be an exact multiple of the fastest growing wavelength ensures that the wavenumber is the analytically calculated n_{max} .

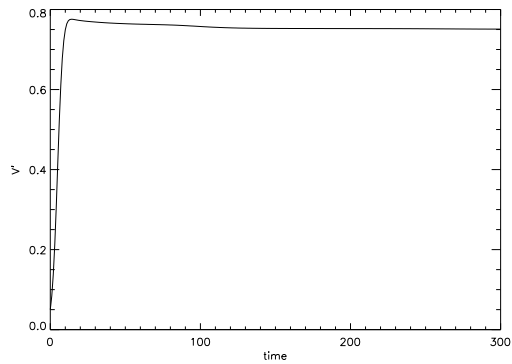


Figure 3. The evolution of $V'(X)$ with stress-free boundary conditions when $\hat{\sigma} = -1$, $\hat{\Omega} = -2/3\hat{\sigma}$, $\hat{\eta} = 1$, $\hat{\nu} = 1$, $v_A = 1$, and $\delta = \epsilon = 0.1$.

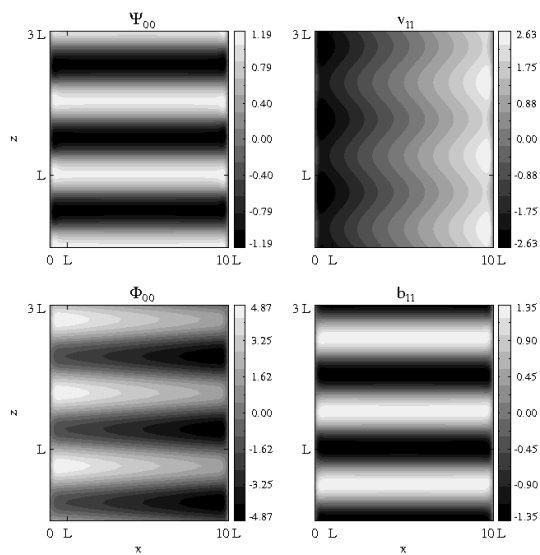


Figure 4. The saturated state reached in figure 3.

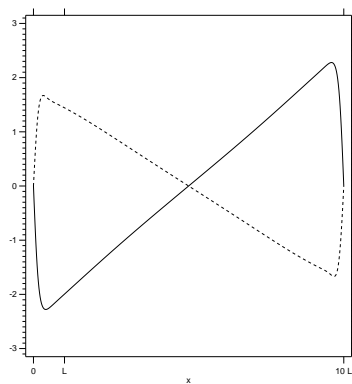


Figure 5. The z -average of v'_{11} (solid) and ϕ'_{00} (dashed) in figure 4. The quantities ψ'_{00} and b'_{11} have zero mean in the z direction.

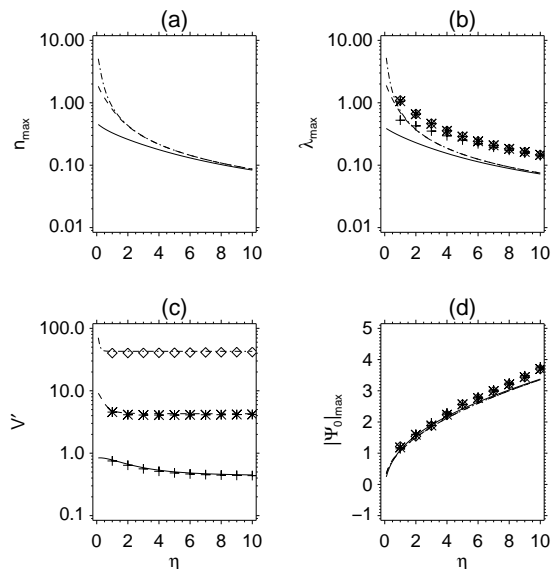


Figure 6. Asymptotic predictions for (a) the wavenumber n_{max} of the fastest growing mode, (b) its growth rate λ_{max} , (c) the resulting shear rate $V'(X)$ and (d) the maximum stream function amplitude predicted by the nonlinear dispersion relation with the computed value at the midpoint $|\Psi_0|_{max} \equiv \max_{0 \leq z \leq N_z L} |\psi'_{00}(L_X/2, z, t_\infty)|$, as functions of $\hat{\eta}$ for $\hat{\Omega} = -2/3\hat{\sigma}$, $\hat{\nu} = 1$, $v_A = 1$ and $\hat{\sigma} = -100, -10, -1$ (dashed-dot, dashed, solid) with superposed numerical results (squares, diamonds, asterisks). The choice of the computational domain to be an exact multiple of the fastest growing wavelength ensures that wavenumber is the analytically calculated n_{max} .

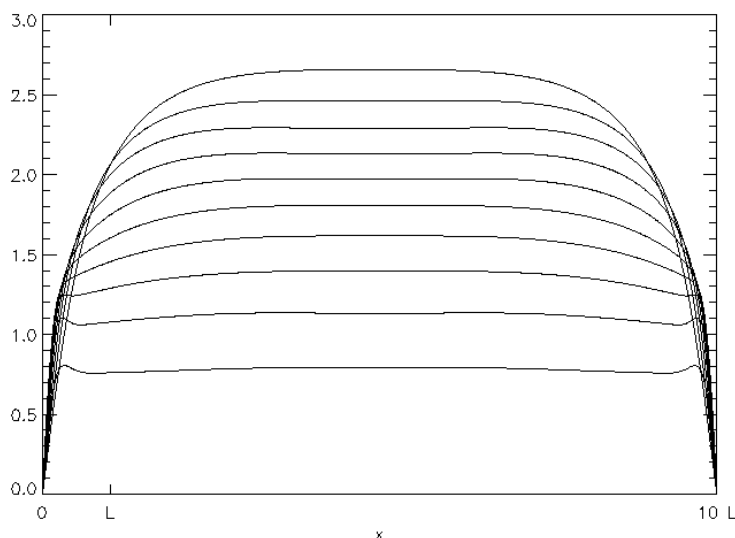


Figure 7. Root-mean-square of ψ'_{00} as a function of $\hat{\eta}$ for integer values from $\hat{\eta} = 1$ (lowest curve) to $\hat{\eta} = 10$ (highest curve) with $\hat{\Omega} = -2/3\hat{\sigma}$, $\hat{\sigma} = -1$, $\hat{\nu} = 1$, $v_A = 1$ and $\delta = \epsilon = 0.1$.

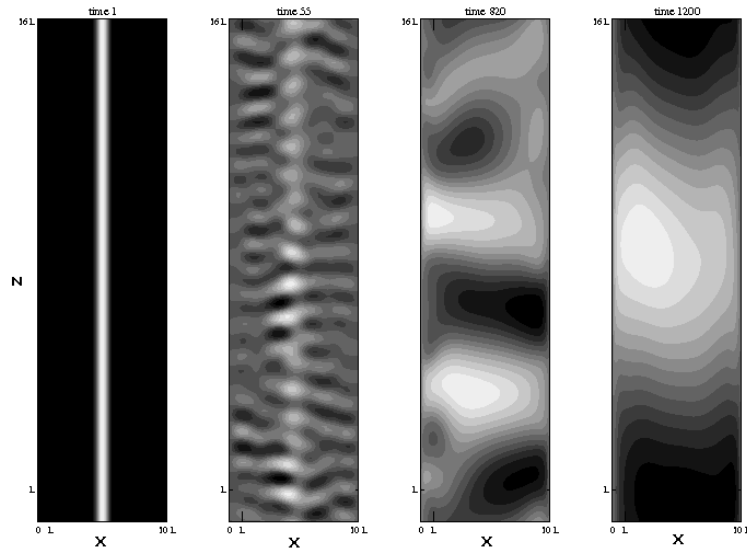


Figure 8. The evolution of ϕ'_{00} from an initial Gaussian profile in x with $\hat{\sigma} = -1$, $\hat{\Omega} = -2/3\hat{\sigma}$, $\hat{\eta} = 1$, $\hat{\nu} = 1$, $v_A = 1$, and $\delta = \epsilon = 0.1$.

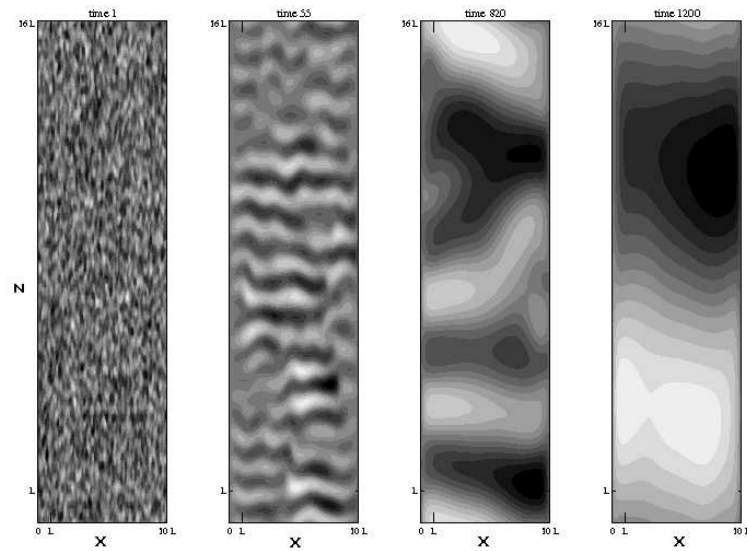


Figure 9. The evolution of ϕ'_{00} starting from small amplitude random initial conditions with $\hat{\sigma} = -1$, $\hat{\Omega} = -2/3\hat{\sigma}$, $\hat{\eta} = 1$, $\hat{\nu} = 1$, $v_A = 1$, and $\delta = \epsilon = 0.1$.

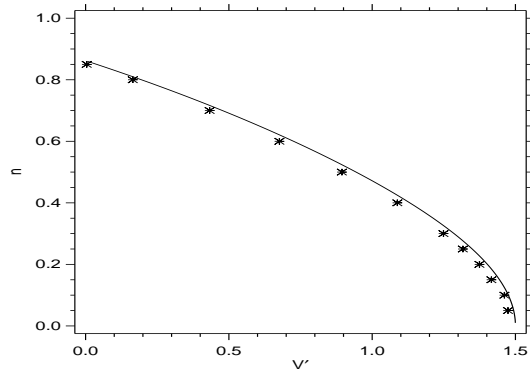


Figure 10. The value of $V'(X)$ for each of the saturated states begun with varying vertical box length L_Z , where $n = 2\pi/L_Z$. The solid line represents the single mode theory from [11], while the asterisks denote numerical results taken after the flow has coarsened to the box-filling wavelength L_Z starting from a random small amplitude perturbation. The parameters are $\widehat{\Omega} = 1$, $\widehat{\sigma} = -1.5$, $\widehat{\nu} = \widehat{\eta} = 1$, $v_A = 1$ and $\delta = \epsilon = 0.1$.

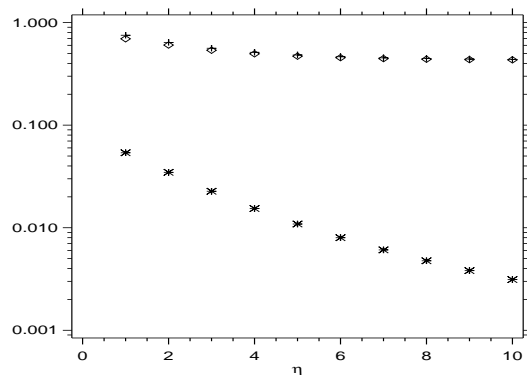


Figure 11. Reynolds and magnetic Reynolds stresses in Eq. (20) for $V'(X)$. The values of $V'(X)$, $-v_A^2 a'_{00} b'_{11} / \widehat{\nu}$, $u'_{00} v'_{11} / \widehat{\nu}$ are represented by crosses, diamonds and asterisks, respectively. Here $\widehat{\eta}$ varies from 1 to 10 while $\widehat{\sigma} = -1$, $\widehat{\Omega} = -2/3\widehat{\sigma}$, $\widehat{\nu} = 1$, $v_A = 1$, and $\delta = \epsilon = 0.1$.